An MHD Modeling of the Successive X2.2 and X9.3 Solar Flares of 2017 September 6

Satoshi Inoue^{1,2} and Yumi Bamba^{2,3}

Center for Solar-Terrestrial Research, New Jersey Institute of Technology, 323 Dr Martin Luther King Jr Blvd., Newark, NJ 07102-1983, USA; si22@njit.edu

Institute for Space-Earth Environmental Research, Nagoya University, Furo-cho, Chikusa-ku, Nagoya, 464-8601, Japan

Institute for Advanced Research, Nagoya University, Furo-cho, Chikusa-ku, Nagoya 464-8601, Japan

Received 2020 May 27; revised 2021 April 12; accepted 2021 April 13; published 2021 June 16

Abstract

The solar active region 12673 produced two successive X-class flares (X2.2 and X9.3) approximately 3 hr apart in 2017 September. The X9.3 flare was the largest recorded solar flare in Solar Cycle 24. In this study we perform a data-constrained magnetohydrodynamic simulation taking into account the observed photospheric magnetic field to reveal the initiation and dynamics of the X2.2 and X9.3 flares. According to our simulation, the X2.2 flare is first triggered by magnetic reconnection at a local site where at the photosphere the negative polarity intrudes into the opposite-polarity region. This magnetic reconnection expels the innermost field lines upward, beneath which the magnetic flux rope is formed through continuous reconnection with external twisted field lines. Continuous magnetic reconnection after the X2.2 flare enhances the magnetic flux rope, which is lifted up and eventually erupts via the torus instability. This gives rise to the X9.3 flare.

Unified Astronomy Thesaurus concepts: Magnetohydrodynamical simulations (1966); Solar flares (1496); Solar magnetic fields (1503); Solar active regions (1974)

Supporting material: animation

1. Introduction

The solar active region (AR) 12673 was observed in 2017 September. The AR first appeared at the end of August and started growing on September 3 and went on to rapidly strengthen its magnetic energy and helicity (Vemareddy 2019). During its evolution, AR 12673 produced X-class flares several times in addition to C- and M-class flares (Yamasaki et al. 2021). One of its solar flares, an X9.3 flare, is the largest recorded solar flare in Solar Cycle 24, which generated not only strong white-light emission but also gamma-ray emission (Lysenko et al. 2019). It eventually produced a geo-effective coronal mass ejection (Wu et al. 2019; Scolini et al. 2020). In addition, an X2.2 flare was observed approximately 3 hr before the X9.3 flare (Mitra et al. 2018; Yan et al. 2018; see also the GOES plot shown in Figure 1(a)), i.e., this AR produced successive X-class flares. AR 12673 exhibited strong shearing and converging flows (Wang et al. 2018) and also rotational motion (Yan et al. 2018) at the flaring site, which are typical features of flare-productive ARs (Toriumi & Wang 2019). Furthermore, throughout the period of occurrence of the X2.2 and X9.3 flares, the negative polarity intruded and eventually penetrated into the opposites polarity region (Yang et al. 2017; Romano et al. 2019; Bamba et al. 2020). From the multiwavelength and the spectroscopic data analysis, the intrusion has been considered to enhance the reconnection responsible for producing the successive X-class flares (Bamba et al. 2020).

A nonlinear force-free field (NLFFF) extrapolation (Wiegelmann & Sakurai 2012; Inoue 2016; Guo et al. 2017) is a useful tool for inferring the structure of a three-dimensional (3D) magnetic field. The magnetic field extrapolations using the photospheric magnetic field as a boundary condition have shown the existence of the highly twisted field lines before the X2.2 and X9.3 flares (e.g., Inoue et al. 2018; Jiang et al. 2018; Liu et al. 2018; Mitra et al. 2018; Yan et al. 2018; Zou et al. 2020). The magnetic configuration has been found to be very complicated, for instance, magnetic flux ropes (MFRs) with different sizes and shapes clustered on

the main polarity inversion line (PIL) that produced the successive X-class flares and together partly construct a double-decker MFR (Hou et al. 2018). The temporal variation in the coronal magnetic structure, particularly the variation of the MFR, has been discussed in relation to the X2.2 and X9.3 flares (Liu et al. 2018; Zou et al. 2019). Because the X2.2 flare was confined, the extrapolations showed highly twisted field lines even after the X2.2 flare while only the less twisted lines remained after the X9.3 flare. Furthermore, a null point, which has been suggested to play an important role in solar flares, was also found near the flaring site in the NLFFF extrapolations (Mitra et al. 2018; Zou et al. 2019), while the intrusion was noticeable in the observation.

Because the NLFFFs give information only on the static state of the magnetic field before and after the flare, we need to interpolate the flare dynamics by using them. In order to reveal the flaring process without depending on the interpolation between the extrapolations, data-constrained/driven magnetohydrodynamic (MHD) simulations have been performed (Inoue et al. 2018; Jiang et al. 2018; Price et al. 2019). The dataconstrained MHD simulation (Inoue et al. 2018) used a snapshot of the photospheric magnetic field as the boundary condition. In this case, they used the NLFFF reconstructed just before the X2.2 flare as the initial condition to a time-dependent simulation. Because the NLFFF already contains free magnetic energy, we can expect it to have the potential to produce a solar flare. The simulations reproduced some observational aspects well (Inoue et al. 2018; Jiang et al. 2018) and have recently been used to investigate the particle motion during the flare by using the MHD fields as the background field (Gordovskyy et al. 2020). On the other hand, the data-driven magnetofrictional simulation (Price et al. 2019) is driven by the time-dependent photospheric magnetic field, using the electric field derived from the time-series photospheric magnetic field data (Lumme et al. 2017). Therefore, the simulation starts much earlier than the flare occurrence time compared to the data-constrained MHD simulation; thus, it allows the energy-accumulating process in the AR to be revealed, too.

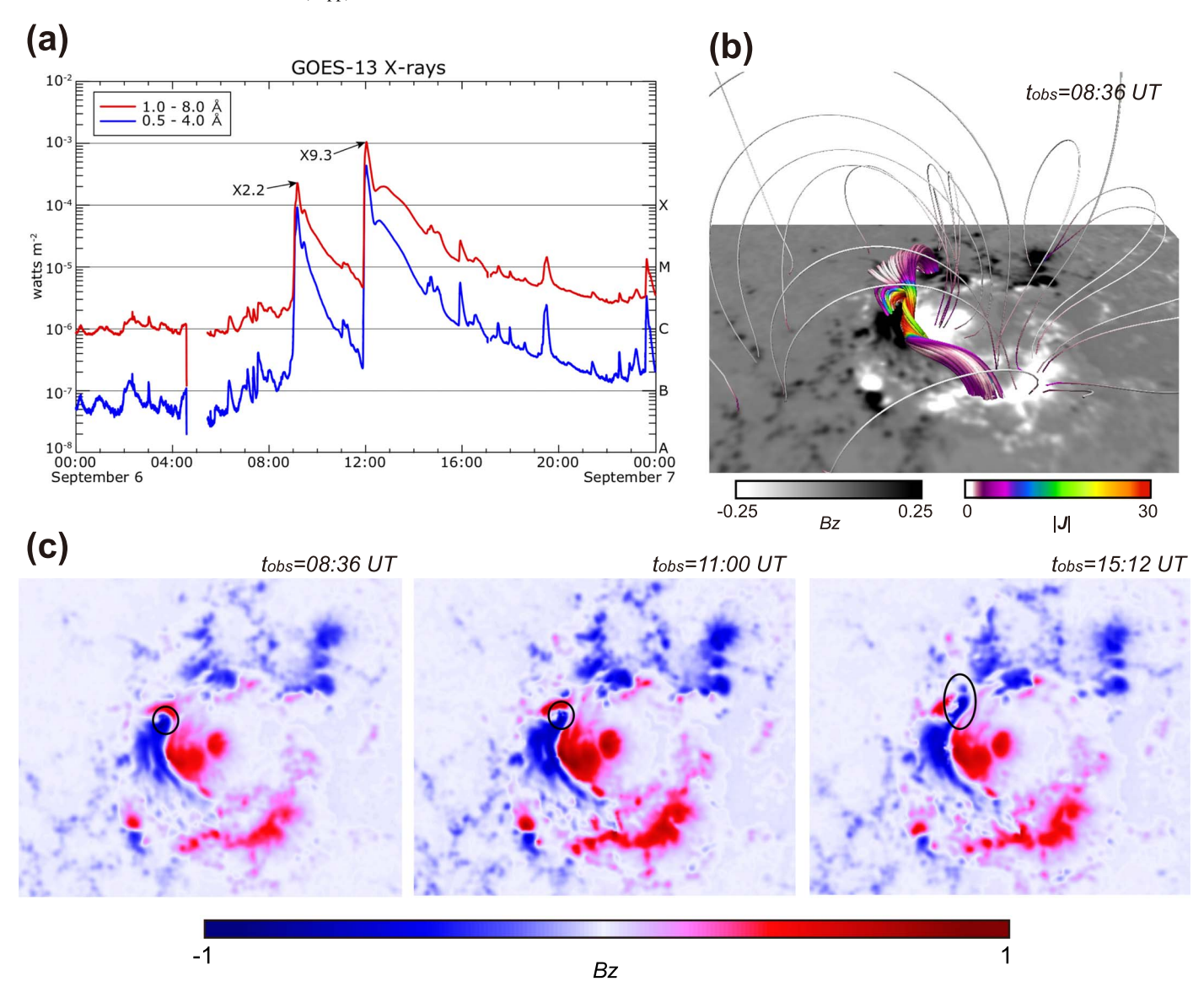


Figure 1. (a) Time profile of the X-ray flux measured by the GOES-13 satellite on September 6. The X2.2 and X9.3 flares indicated by the arrows started at 08:57 UT and 11:53 UT, respectively. The 0.5–4.0 Å passbands and the solar X-ray outputs at 1-8 Å are plotted. (b) Three-dimensional magnetic field reconstructed under an NLFFF approximation based on the photospheric magnetic field. The photospheric magnetic field is obtained at 08:36 UT on September 6, which is 20 minutes before the X2.2 flare. The color of the field lines indicates the strength of the current density |J|. (c) The photospheric magnetic field (normal component) is shown at $t_{\rm obs} = 08:36$ UT, $t_{\rm obs} = 11:00$ UT, and $t_{\rm obs} = 15:12$ UT, respectively. The panels cover the time from before the X2.2 flare observed at 08:57 UT to after the X9.3 flare observed at 11:53 UT. Throughout the X2.2 and X9.3 flares, the negative magnetic field indicated by the black circles intrudes into the positive polarity region and eventually penetrates it.

Note that the results just imitate the observations because most of these simulations assume a simple solar atmosphere (for instance, no chromosphere) and stay in the MHD framework without a radiative transfer process.

In our previous paper (Inoue et al. 2018), we reported on the simulation results for the eruption in which multiple twisted lines are merged through reconnection, resulting in the large erupting MFR, and we discussed the dynamics of the erupting MFR. On the other hand, the detailed initiation mechanism, the reason, and mechanism of the successive huge X-class flares are not fully understood. In this study, we analyzed the simulation data together with observational data in detail to reveal the onset mechanism to produce both the X2.2 and X9.3 flares. The rest of this paper is constructed as follows: the observations and numerical method are described in Section 2, results and discussion are presented in Sections 3 and 4, and our conclusion is summarized in Section 5.

2. Numerical Method and Observations

2.1. Numerical Method

The numerical method is largely the same as the one described in our previous study (Inoue et al. 2018). In the following we shortly summarize its main aspects. Both the NLFFF extrapolation method and the MHD simulation are based on the zero-beta MHD approximation given by the following equations:

$$\rho(\mathbf{x}, t) = |\mathbf{B}(\mathbf{x}, t)|,\tag{1}$$

$$\frac{\partial \mathbf{v}}{\partial t} = -(\mathbf{v} \cdot \nabla)\mathbf{v} + \frac{1}{\rho}\mathbf{J} \times \mathbf{B} + \nu_i \nabla^2 \mathbf{v}, \tag{2}$$

$$\frac{\partial \boldsymbol{B}}{\partial t} = \boldsymbol{\nabla} \times (\boldsymbol{v} \times \boldsymbol{B} - \eta_{i} \boldsymbol{J}) - \boldsymbol{\nabla} \phi, \tag{3}$$

$$\boldsymbol{J} = \boldsymbol{\nabla} \times \boldsymbol{B},\tag{4}$$

$$\frac{\partial \phi}{\partial t} + c_{\rm h}^2 \nabla \cdot \mathbf{B} = -\frac{c_{\rm h}^2}{c_{\rm p}^2} \phi,\tag{5}$$

where the formulation of viscosity and resistivity are different in the NLFFF and MHD computations, respectively. Therefore, the subscript i of η and ν corresponds to "NLFFF" or "MHD." The length, magnetic field, density, velocity, time, and electric current density are normalized by $L^* = 244.8$ (Mm), $B^* = 0.25$ (T), $\rho^* = |B^*|$ (kg m $^{-3}$), and $V_A^* \equiv B^*/(\mu_0 \rho^*)^{1/2}$ (m s $^{-1}$), where μ_0 is the magnetic permeability, $\tau_A^* \equiv L^*/V_A^*$ (s), and $J^* = B^*/\mu_0 L^*$ (A m $^{-2}$), respectively. ϕ is an artificial scalar potential used for controlling the errors from $\nabla \cdot \boldsymbol{B}$ (Dedner et al. 2002), with the coefficients c_h^2 and c_p^2 in Equation (5) fixed to the constant values 0.04 and 0.1, respectively. The initial condition of density is given by $\rho(t=0, \boldsymbol{x}) = |\boldsymbol{B}(t=0, \boldsymbol{x})|$, and the velocity is set to zero in all space in the NLFFF calculation and also MHD simulation.

A numerical box of $244.8 \times 158.39 \times 195.84$ (Mm³), which is given as $1 \times 0.674 \times 0.8$ in its nondimensional value, is divided by $340 \times 220 \times 272$ grid points. The data used in this study are obtained through a $2 \times 2 \times 2$ binning process of the original SHARP data. The photospheric magnetic field is preprocessed according to Wiegelmann et al. (2006). This process attempts to minimize L, which is the sum of the total force L_1 , the total torque L_2 , the difference between the updated magnetic field and observed one L_3 , and the smoothing L_4 , as follows:

$$L = \mu_1 L_1 + \mu_2 L_2 + \mu_3 L_3 + \mu_4 L_4,$$

$$L_1 = \left(\sum B_x B_z\right)^2 + \left(\sum B_y B_z\right)^2 + \left(\sum B_z^2 - B_x^2 - B_y^2\right)^2,$$

$$L_2 = \left(\sum x (B_z^2 - B_x^2 - B_y^2)\right)^2 + \left(\sum y (B_z^2 - B_x^2 - B_y^2)\right)^2 + \left(\sum y B_x B_z - x B_y B_z\right)^2,$$

$$L_3 = \sum (B_x - B_{x,\text{obs}})^2 + \sum (B_y - B_{y,\text{obs}})^2 + \sum (B_z - B_{z,\text{obs}})^2,$$

$$L_4 = \sum (\Delta B_x^2 + \Delta B_y^2 + \Delta B_z^2).$$

In this study, $\mu_1 = \mu_2 = 1.0$ and $\mu_3 = \mu_4 = 1.0 \times 10^{-2}$ are used.

2.1.1. Nonlinear Force-free Field Extrapolation

Details of the NLFFF extrapolation method are described in our previous studies (Inoue et al. 2014, 2018, 2018). In particular, the parameters used in this study are the same as those in our previous study (Inoue et al. 2018). The viscosity and resistivity are given as $\nu_{\rm nlfff}=1.0\times 10^{-3}$ and $\eta_{\rm nlfff}=\eta_0+\eta_1|{\bf J}\times{\bf B}||{\bf v}|^2/|{\bf B}|^2$, respectively, where $\eta_0=5.0\times 10^{-5}$ and $\eta_1=1.0\times 10^{-3}$ in nondimensional units. The second term is introduced to enhance reconnection, which helps to make the highly twisted lines observed in a central area of active regions. Furthermore, because the resistivity is proportional to the Lorentz force, it accelerates the relaxation of the nonequilibrium magnetic field toward the forcefree state. The potential field is given as the initial condition, which is extrapolated using the Green function method (Sakurai 1982). During the iteration, three components of the magnetic field are fixed at each boundary, while the velocity is fixed to zero and the von Neumann condition $\partial/\partial n=0$ is imposed on ϕ . Note

that the bottom boundary is fixed according to

$$\mathbf{B}_{bc} = \zeta \mathbf{B}_{obs} + (1 - \zeta) \mathbf{B}_{pot},$$

where B_{bc} is the transverse component determined by a linear combination of the observed magnetic field (B_{obs}) and the potential magnetic field (B_{pot}) . ζ is a coefficient in the range of 0 to 1. When $R = \int |J \times B|^2 dV$, which is calculated over the interior of the computational domain, falls below a critical value denoted by R_{min} , during the iteration, the value of the parameter ζ is increased to $\zeta = \zeta + \mathrm{d}\zeta$. In this paper, R_{min} and $\mathrm{d}\zeta$ have the values 1.0×10^{-2} and 0.02, respectively. If ζ is equal to 1, B_{bc} is completely consistent with the observed data. Furthermore, the velocity is controlled as follows. If the value of $v^*(=|v|/|v_A|)$ is larger than v_{max} (here set to 0.02), then the velocity is modified as follows: $v \Rightarrow (v_{max}/v^*)v$. These processes would help avoid a sudden jump from the boundary into the domain during the iterations.

The NLFFFs are reconstructed from the photospheric magnetic field obtained at 02:36 UT and 08:36 UT on September 6. Figure 1(b) shows the 3D magnetic field of the NLFFF at 08:36 UT. The strongly twisted lines have a strong current density while the overlying field lines take a state close to the potential field. The comparison with the extreme ultraviolet image and how much the magnetic field satisfies the force-free state are described in the Appendix to Bamba et al. (2020).

2.1.2. Magnetohydrodynamic Simulation

The zero-beta MHD simulations are carried out using the NLFFFs as the initial conditions, which are reconstructed at 08:36 UT and 02:36 UT on September 6, respectively, and hereafter denoted Runs A and B. The resistivity and viscosity are set to a uniform $\eta_{\rm mhd}=1.0\times 10^{-5}$ and $\nu_{\rm mhd}=1.0\times 10^{-4}$. The density is initially given as $\rho(x, t = 0) = |B(x, t = 0)|$. Even during the MHD simulation, we imposed $\rho(\mathbf{x}, t) = |\mathbf{B}(\mathbf{x}, t)|$; however, the dynamics in the lower corona as focused on in this study are not so different from those obtained using a mass conservation law equation (Amari et al. 1999; Inoue et al. 2014). Note that there is no physical significance for the density obtained in this simulation. The density is fixed at boundaries during the calculation. The normal component B_n is fixed at all boundaries but the transverse component B_t , derived from an induction equation under the velocity, equals zero, and η is also fixed at zero at each boundary. For instance, at the bottom surface, the time variations of B_x and B_y are derived from

$$\frac{\partial B_x}{\partial t}|_{z=0} = \frac{\partial E_y}{\partial z} - \frac{\partial \phi}{\partial x},\tag{6}$$

$$\frac{\partial B_{y}}{\partial t}|_{z=0} = -\frac{\partial E_{x}}{\partial z} - \frac{\partial \phi}{\partial y},\tag{7}$$

where $E_x = (\eta_{\text{mhd}} \boldsymbol{J} - \boldsymbol{v} \times \boldsymbol{B})_x$ and $E_y = (\eta_{\text{mhd}} \boldsymbol{J} - \boldsymbol{v} \times \boldsymbol{B})_y$ are the *x* and *y* components of the electric field. The boundary conditions of the other variables are identical to those in the NLFFF calculation.

2.2. Observations

To reconstruct the NLFFFs, we use the photospheric magnetic field obtained at 02:36 UT and 08:36 UT, which

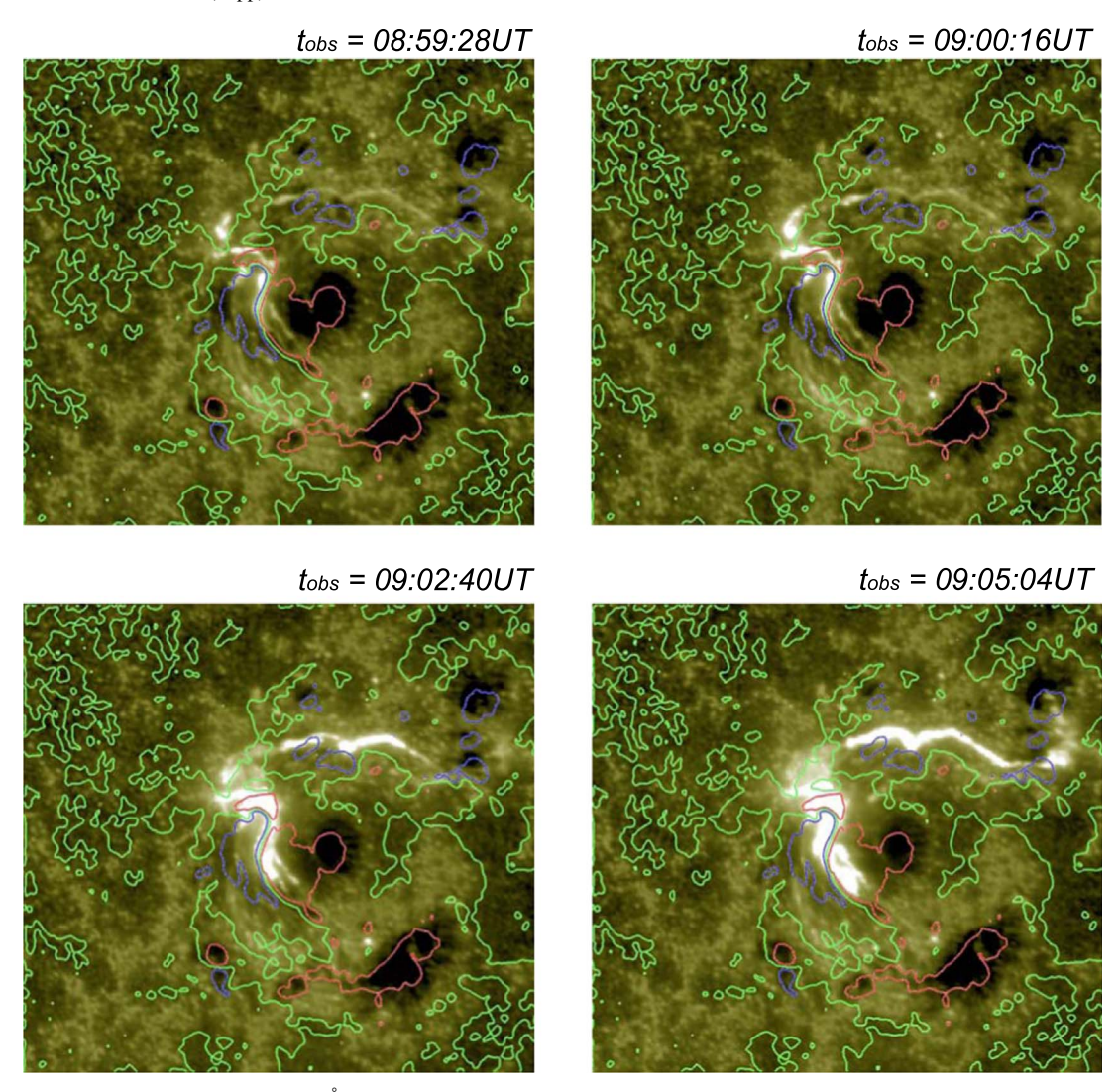


Figure 2. The images are obtained from AIA 1600 Å during the X2.2 flare. The red and blue lines correspond to the contours of $B_z = 0.25$ and $B_z = -0.25$, respectively. The green lines represent the polarity inversion lines.

are 6 hr 20 minutes and 20 minutes before the X2.2 flare, respectively, on September 6 taken by the Helioseismic and Magnetic Imager (HMI; Scherrer et al. 2012) on board the Solar Dynamics Observatory (SDO; Pesnell et al. 2012). This observation is shown in the space-weather HMI active region patch format (Bobra et al. 2014). The far-ultraviolet (FUV) 1600 Å image taken by the Atmospheric Imaging Assembly (AIA; Lemen et al. 2012) on board the SDO is also used to compare with the NLFFF and dynamics obtained from the simulation.

As outstanding features, the negative polarity intrudes and eventually penetrates into the positive polarity during the successive flares as shown in Figure 1(c). For instance, Bamba et al. (2020) suggest that the reconnection is enhanced there, which would be important in causing the successive flares. Figures 2 and 3 show the AIA 1600 images obtained during the X2.2 and X9.3 flares. In both cases, strong brightening is observed at the PIL where the strong twisted lines exist as seen in Figure 1(b). Although both profiles are similar, the X9.3 flare shows stronger enhancement and the brightening further extends southward along the PIL.

3. Results

3.1. Initiation of the X2.2 Flare

Figure 4(a) shows an FUV 1600 Å image taken by AIA at the time that corresponds to the onset of the X2.2 flare. In Figure 4(b), a selection of field lines traced from the MHD simulation at t = 0.28 when the reconnection starts is superimposed on this image, in which their footpoints are anchored well to the strong brightening sites (see also the inset in Figure 4(b)). Therefore, those field lines induce the X2.2 flare. Figure 4(c) shows the side view of the field lines where the color of the line corresponds to the value of |J|/|B|. We found the strong current density indicated by the circle to be located directly above the region where the negative polarity intrudes into the opposite-polarity region. In the very early stage of the simulation (Figures 4(c)-(d)), magnetic reconnection occurs, resulting in new twisted lines. Note that because the horizontal magnetic field at the photosphere changes according to Equations (6) and (7) in the MHD simulation, the magnetic field gradually deviates from the NLFFF at t=0following which the magnetic field above changes because the NLFFF cannot take a perfect force-free state that causes the

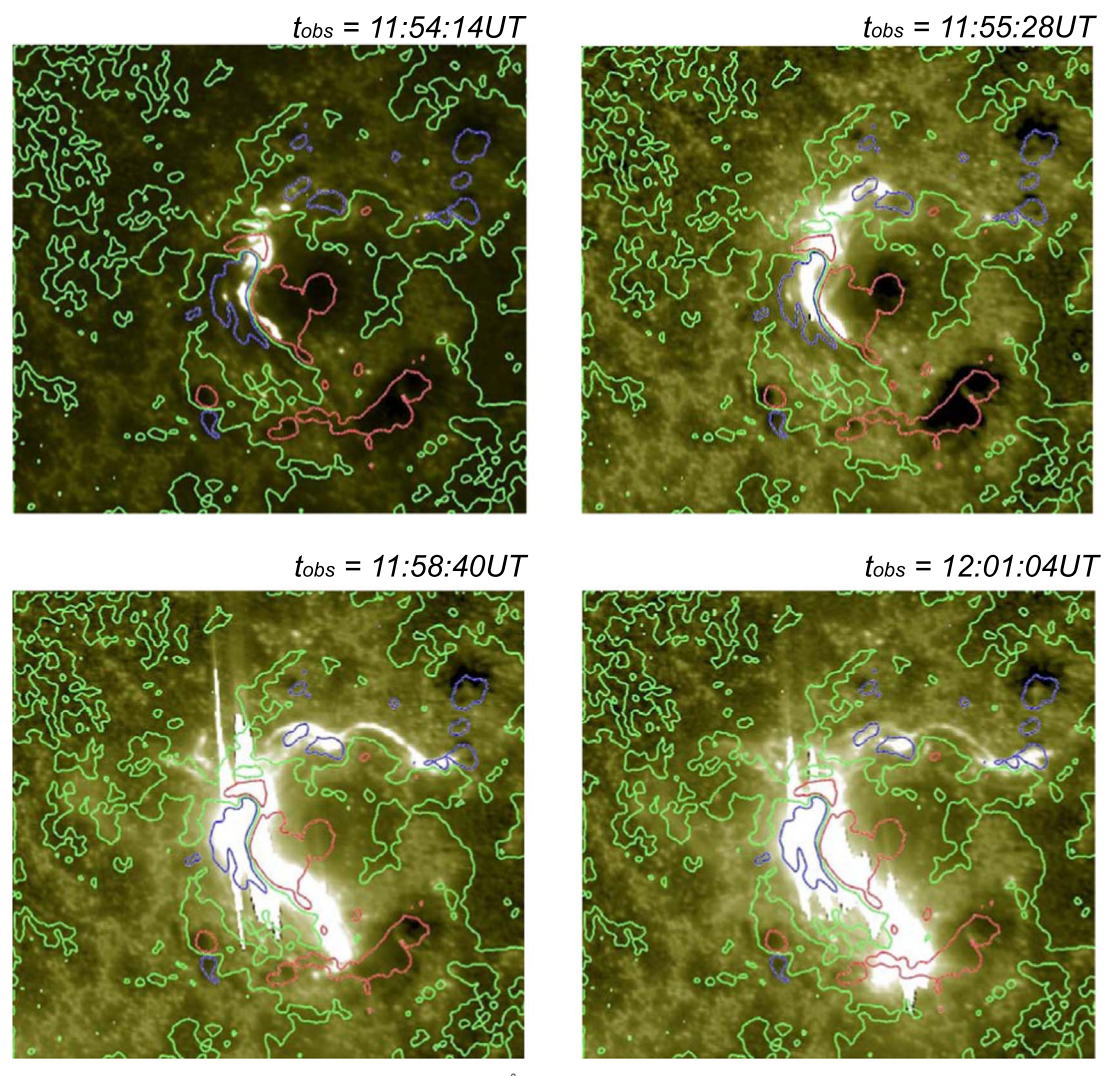


Figure 3. The images are taken from AIA 1600 Å during the X9.3 flare. The format is the same as Figure 2.

residual force to act on the magnetic field. In addition the velocity limit imposed in the NLFFF calculation is deactivated, and consequently, reconnection is excited in the MHD simulation while the NLFFF keeps the configuration as shown in Figure 1(b).

The vertical cross section shown in Figures 4(c) and (d) shows the decay index n. The decay index (Bateman 1978; Kliem & Török 2006) is defined as

$$n = -\frac{z}{B_{p_i}} \frac{\partial B_{p_i}}{\partial z},\tag{8}$$

where B_{p_i} denotes the horizontal component of the external field surrounding the MFR. Here, we assume a potential field as the external field. This value is a proxy of the torus instability (TI; Kliem & Török 2006). When the axis of the MFR reaches the region in red where the condition $n \ge 1.5$ is satisfied, TI works on the MFR, i.e., the upward hoop force due to the current flowing inside the MFR is dominant over the strapping force from the external field. Note that the threshold strongly depends on the shape or boundary condition of the MFR (Olmedo & Zhang 2010; Zuccarello et al. 2015) and mass sustained by the MFR (Jenkins et al. 2019). We found that the twisted lines formed through reconnection cannot reach the

region where those become unstable to the TI. Therefore, we suggest that the MFR at this time is stable to the TI.

We already discussed the possibility of the onset driven by kink instability (KI) in Inoue et al. (2018). According to their results, the highly twisted lines that satisfy the KI (Török et al. 2004) are not found in the NLFFF (see also Figure 9 in this paper), and the possibility of KI is low even in the highly twisted erupting MFR created through the reconnection. Therefore, we rule out KI as an initiation mechanism for this event.

Figure 4(e) shows the AIA 94 Å image when the X2.2 flare just starts. The strong brightening area is observed along with the PIL marked by the yellow dashed circle. The field lines are plotted over the AIA 94 Å image in Figure 4(f) where the color is in the same format as the one in Figures 4(c) and (d) and the reconnection starts at t = 0.28 in the simulation at the same area. Therefore, the observation supports that the initiation is triggered by the reconnection at the strong current region formed by the intruding motion of the sunspot.

3.2. Three-dimensional Dynamics of the Magnetic Field

Figure 5(a) plots the field lines causing the X2.2 flare again, as well as another set of twisted lines that do not participate in the onset of the X2.2 flare. The X2.2 flare is triggered by

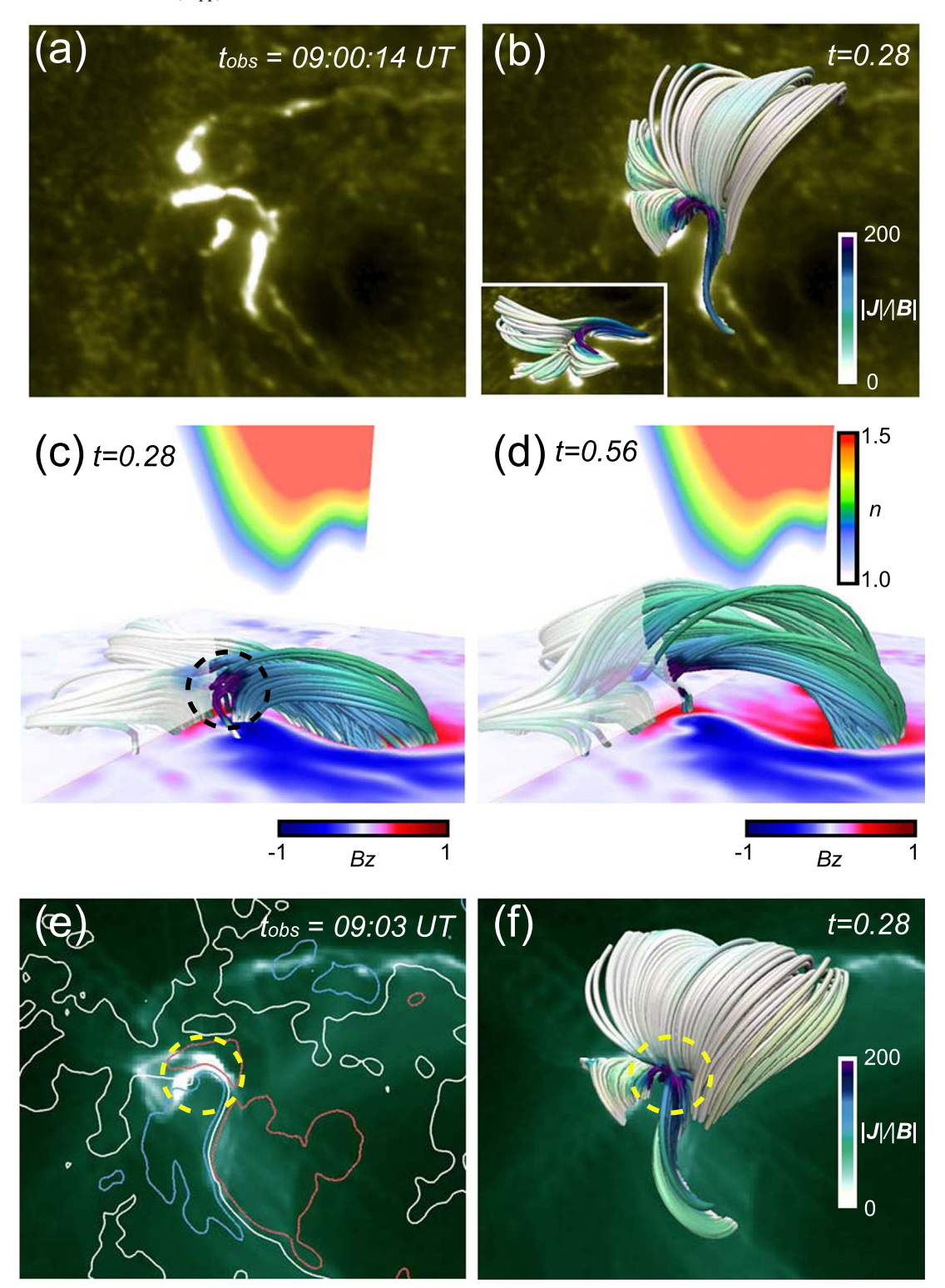


Figure 4. (a) AIA 1600 Å image at 09:00 UT at the onset phase of the X2.2 flare. (b) Field lines obtained from the MHD simulation at t = 0.28, when the reconnection starts, are superimposed on the AIA image for the run where the initial condition given by the NLFFF is reconstructed at 08:36 UT. The color of the field lines corresponds to the value of |J|/|B|. The small inset is the side view. (c)–(d) The onset of the X2.2 flare is inferred from the simulation. The field lines are plotted obtained from the MHD simulation at t = 0.28 and t = 0.56, respectively. These field lines would induce the X2.2 flare. The bottom panel shows the B_z distribution, and the decay index value is painted on the vertical cross section in a range from 1.0 to 1.5. (e) AIA 94 Å image at 09:03 UT at the onset phase of the X2.2 flare with contours of $B_z = \pm 0.25$ and PIL in red (+), blue (-), and white, respectively. Strong brightening area is marked by the yellow dashed circle. (f) The field lines are plotted over the AIA 94 Å image where the color corresponds to |J|/|B|. The yellow dashed circle is the same as the one in (e).

reconnection in the local site indicated by the square and generates long twisted lines as shown in Figure 5(b). This reconnection plays a role in expelling a part of the twisted lines

that exist along the PIL. As a result, another set of twisted lines, which exists at the outside, starts reconnecting under the long twisted lines that are formed in an early phase of the X2.2 flare,

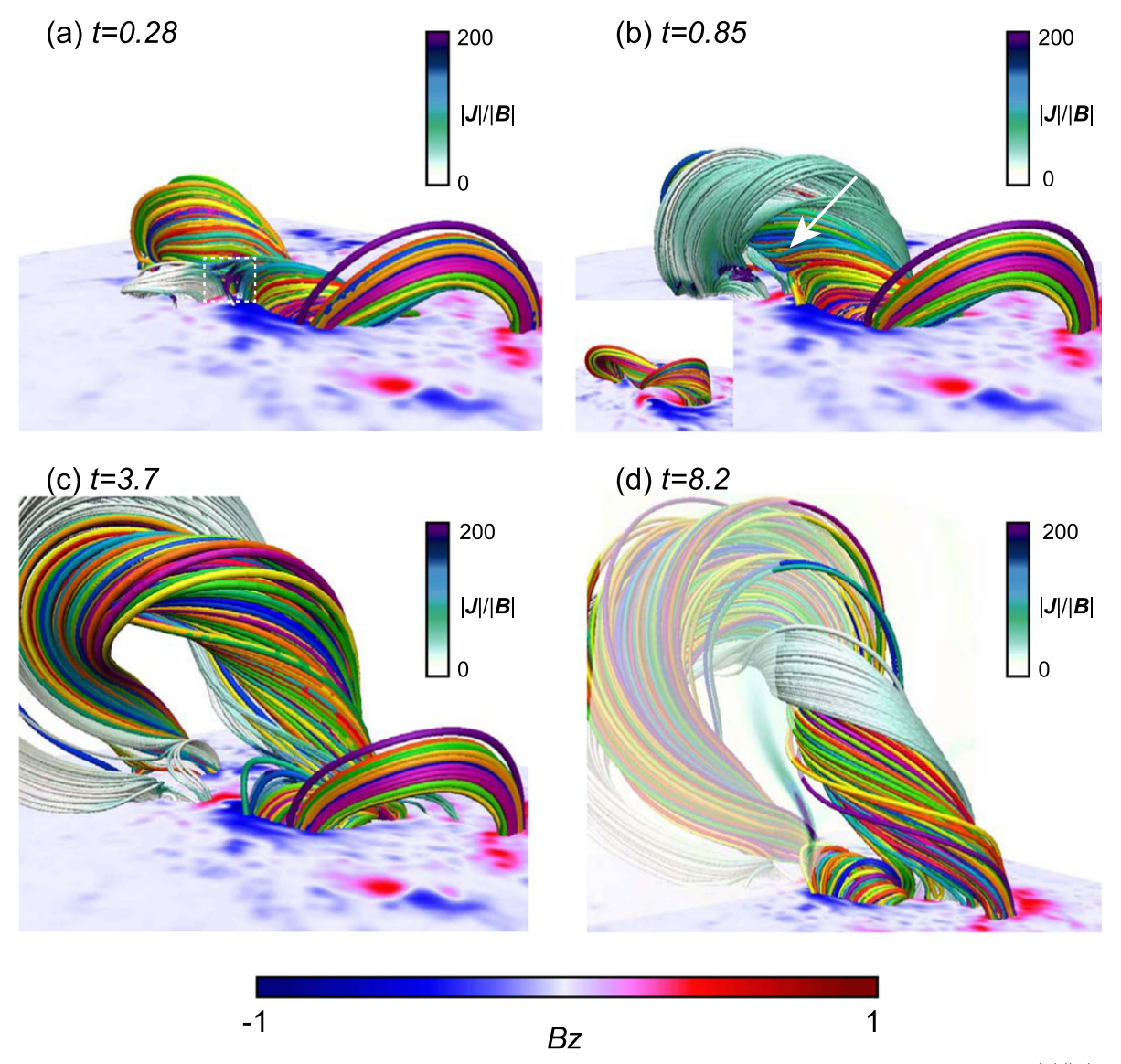


Figure 5. (a)—(d) The temporal evolution of the magnetic field lines causing the X2.2 and X9.3 flares. The field lines highlighted by the value of |J|/|B| correspond to those that are related to the onset of the X2.2 flare. The format is the same as in Figure 1. Another set of field lines that belong to a large erupting MFR inducing the X9.3 flare is shown. The vertical cross section in (d) is plotted using the |J|/|B| distribution. The arrow shown in (b) points toward the newly created MFR, whose enlarged view is in the inset. An animation of this figure is available. It shows the sequence from t=0 to 8.2. The realtime duration of the animation is 4 seconds. (An animation of this figure is available.)

as shown in Figure 5(b). The inset of Figure 5(b) shows an enlarged view of the newly created MFR indicated by the arrow. Continuous reconnection takes place below the MFR, which supplies the twist and makes the MFR bigger (later discussed), eventually causing the eruption that triggers the X9.3 flare (Figures 5(c)–(d)). Figure 2 shows that, after the initial brightening at $t_{\rm obs} = 09:00$ UT, the brightening is further enhanced around the PIL. Therefore, the reconnection still occurs around the PIL. The simulation in this study proves that the reconnection is caused by the sheared field lines under the twisted lines created at the onset stage of the X2.2 flare. This reconnection generates a fundamental MFR as shown in the inset of Figure 5(b), which evolves into the large MFR via the subsequent reconnection and leads to the X9.3 flare.

We compare the erupting MFR and current density |J| (or |J|/|B|) with the AIA 1600 Å image obtained during the X9.3 flare.

Figure 6(a) shows an erupting MFR with the AIA 1600 Å image projected onto the simulation bottom, which is taken at 12:01:04 UT. The observational time $t_{\text{obs}} = 12:01:04$ UT of AIA 1600 Å is just after the strongest brightening of the X9.3 flare, which we interpret as the time at which the MFR goes up away from the AR. Therefore, we select the last time of the simulation for the comparison. By comparing between the AIA images obtained during the X2.2 and the X9.3 flares shown in Figures 2 and 3, we find that the brightening related to the X9.3 flare extends farther to the south along the PIL compared to the case for the X2.2 flare. In this simulation, one leg of the erupting MFR is anchored in the extended brightening region. Figure 6(b) focuses on the lower area beneath the erupting MFR. The current sheet is formed above postflare loops, whose footpoints are anchored in the intense brightening region shown in the AIA image. Because a bifurcation of up- and downflows is present close to the current sheet, we

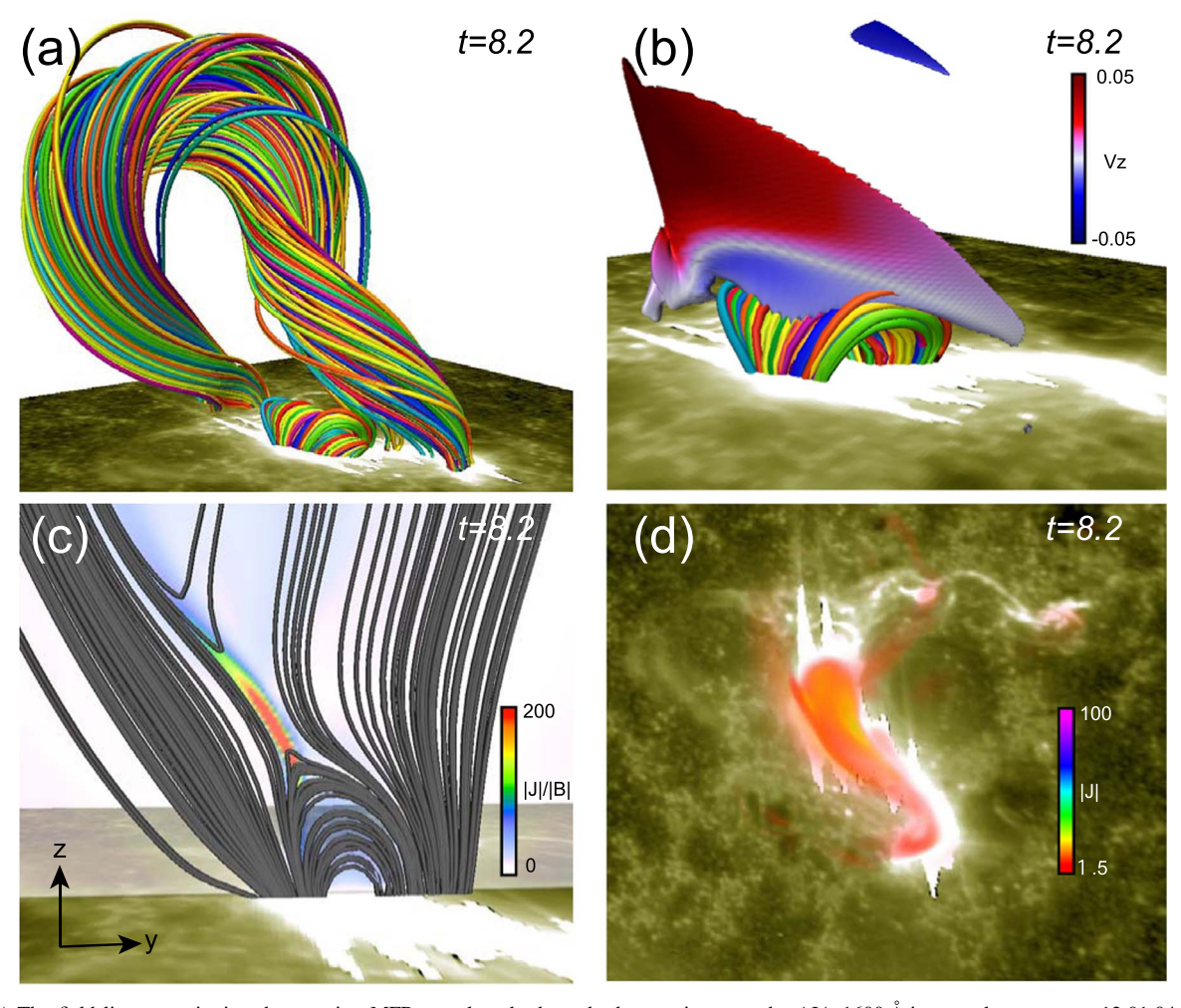


Figure 6. (a) The field lines constituting the erupting MFR are plotted where the bottom is set as the AIA 1600 Å image taken at $t_{\rm obs} = 12:01:04$ UT on 2017 September 6. (b) The enlarged view close to the surface under the erupting MFR where the AIA 1600 Å image set at the bottom is the same as in (a). The surface corresponds to the isosurface of |J|/|B| = 80 where the color represents v_z . (c) The field lines in gray are traced in the y-z plane where the |J|/|B| is plotted in the vertical cross section. (d) The volume rendering of |J| is superimposed on the AIA 1600 Å image.

suggest that the reconnection takes place there. Figure 6(c) plots field lines that are traced in the y-z plane to facilitate the description of the dynamics by reducing it into two-dimensional space. This figure clearly shows that the current sheet is surrounded by antiparallel field lines, which is consistent with the classical standard flare model (e.g., see Priest & Forbes 2002, and its 3D generalization, see, e.g., Aulanier et al. 2012; Janvier et al. 2013). Figure 6(d) plots the volume rendering of current density |J| on the AIA 1600 Å image. The distribution of |J|precisely captures the brightening area enhanced in the AIA 1600 Å image. Therefore, our simulation would produce the MHD process of both the X2.2 and X9.3 flares. On the other hand, the brightening that appears on the northern side is not reproduced in our simulation. One of the reasons that the initial NLFFF does not reproduce the magnetic field in the northern area is because the magnetic field is weaker than that in the central area (Lin et al. 2020).

From these results, we concluded that the X2.2 flare is driven by the reconnection that takes place at the location indicated by the dashed circle in Figure 4(c), while the reconnection drives the X9.3 flare at the strong current region that is located above the PIL as shown in Figure 6(b). Because the size of the regions where the energy is released through the magnetic reconnection

is much different between the first and second flares, our simulation is therefore consistent with the fact that the second flare was bigger than the first one.

3.3. Initiation of the X9.3 Flare

3.3.1. Temporal Evolution of the Height and Velocity of the Erupting MFR

To find out the start of the X9.3 flare, the initiation of the eruption of the large MFR should be discussed because of the association of the flare with the eruption of the MFR. We trace the temporal evolution of the field line in black, shown in Figure 7(a), which is one of the components of the erupting MFR, to understand the transition from pre- to post-eruption of the MFR. Figure 7(b) shows the temporal evolution of the height of the erupting MFR in red and the magnetic flux where the magnetic twist (T_w) of the field lines satisfies $T_w \leqslant -1.0$ in blue. The magnetic twist (Berger & Prior 2006) is defined as

$$T_{w} = \frac{1}{4\pi} \int \frac{\nabla \times \mathbf{B} \cdot \mathbf{B}}{|\mathbf{B}|^{2}} dl, \tag{9}$$

where dl is a line element of a field line. Note that, in this study, the twist is calculated under the condition $|B_z| > 2.5 \times 10^{-3} T$

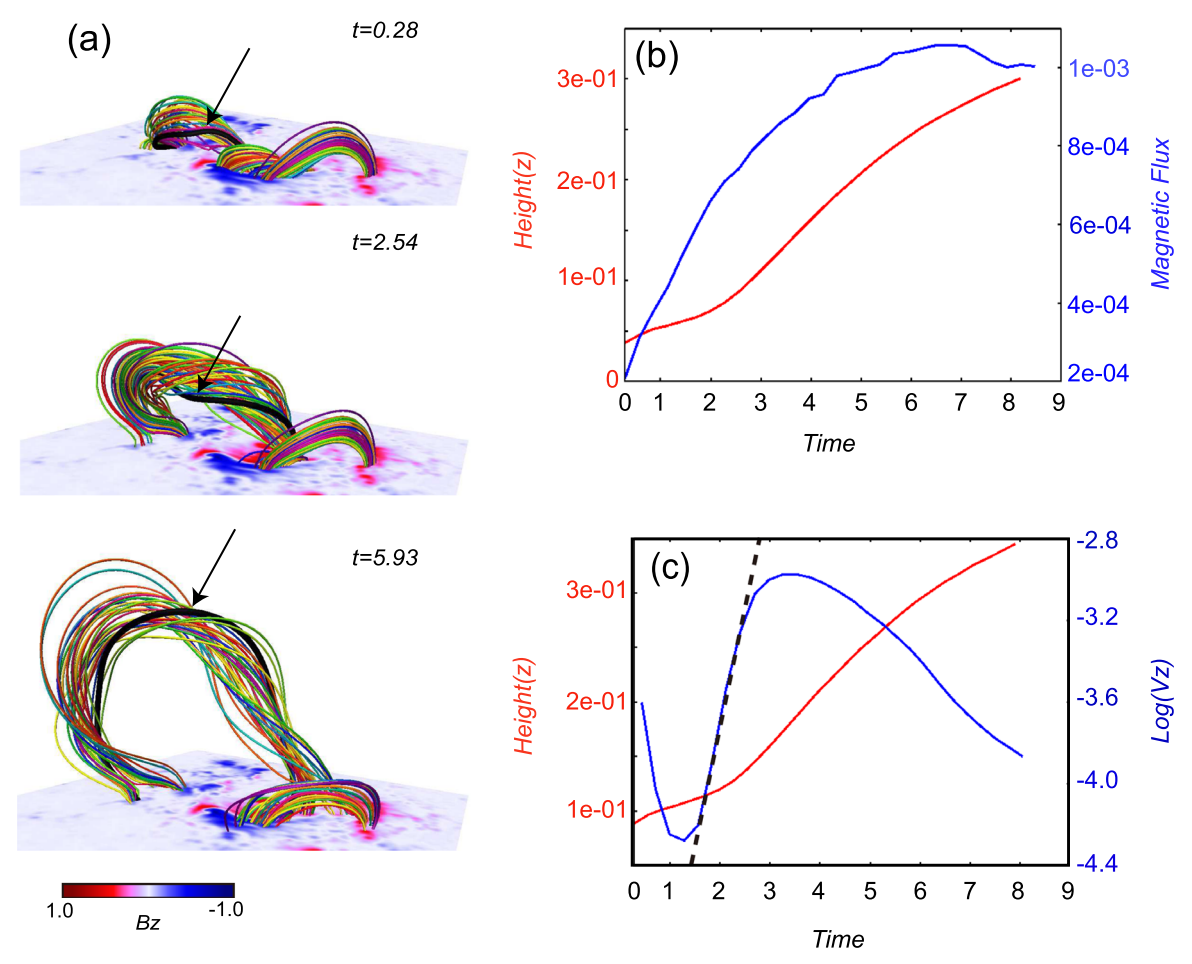


Figure 7. (a) Temporal evolution of the erupting MFR. We temporally trace the black line (indicated by the black arrow), which is one of the components of the erupting MFR. We put a particle at the point r = (0.392, 0.35, 0.039) at t = 0.28 and trace the particle during the simulation. (b) Temporal evolution of the height of the erupting MFR denoted in red and the magnetic flux that satisfies $T_w \le -1.0$ denoted in blue. (c) Temporal evolution of the velocity of the MFR in blue added to the height profile in red. The dashed line represents the exponential growth phase of the velocity.

on the surface. Because T_w measures the number of turns of two infinitesimally close field lines, the twist is strictly different from the winding number of the field line around the magnetic axis of the MFR (Liu et al. 2016; Threlfall et al. 2018). In Figures 7(b) and (c), $t \sim 0$ corresponds to the onset time of the X2.2 flare. The height profile shows a slow-rising phase, $t \leqslant 2$, and a fast-rising phase, $t \geqslant 2$, both of which are typical profiles of the erupting MFR. From Figures 7(b) and (c) we can thus deduce that the X9.3 flare starts around $t \sim 2$ when the MFR shifts to the fast-rising mode. During the slow-rising phase, the size of the MFR, which is occupied with $T_w \leqslant -1.0$, increases, i.e., reconnection constantly takes place after the X2.2 flare. Therefore, a pre-eruption MFR is produced through the X2.2 flare and by the continuous reconnection in the slow-rising phase, until the MFR is accelerated.

We also attempt to answer the fundamental question of what mechanism drives the rapid acceleration of the MFR. Figure 7(c) plots the temporal evolution of the velocity of the erupting MFR in blue, in addition to the height profile in red, which is the same as the one shown in Figure 7(b). The velocity is plotted on a log scale, in which it grows linearly during t = 1.5 to ~ 2.5 . Because this period covers the bifurcation from the slow- to fast-rising phase, an instability drives the eruption.

Note that after $t \approx 4$, the velocity gradually decreases because the side boundary suppresses the dynamics of the MFR. Figures 8(a)–(c) present the snapshots of the 3D field lines from the end of the slow-rising phase to the start of the fast-rising phase (i.e., initiation of the MFR), respectively, with the decay index plotted on the vertical cross section. At t = 1.4, a part of the flux rope enters the region where the instability would be triggered in idealized conditions ($n \ge 1.5$). At t = 2.54, further twisted lines, which are enhanced by the reconnection, enter the region of instability. Therefore, this result suggests that the X9.3 flare is driven by TI, which is consistent with the results analyzed by the NLFFF extrapolations performed by Zou et al. (2020).

3.3.2. Comparison of an Evolution of the MFR with AIA Images

We compare the evolution of the magnetic field at the time of the initiation of the X9.3 flare with SDO/AIA observations. The bottom of Figure 8(d) is set at the AIA 1600 Å image taken at the very early stage of the X9.3 flare. These results suggest that the brightening in AIA 1600 Å is enhanced at the time corresponding to when the erupting MFR is formed through the reconnection and gradually arises because the field lines whose footpoints anchored in the brightening areas are changing to the long field

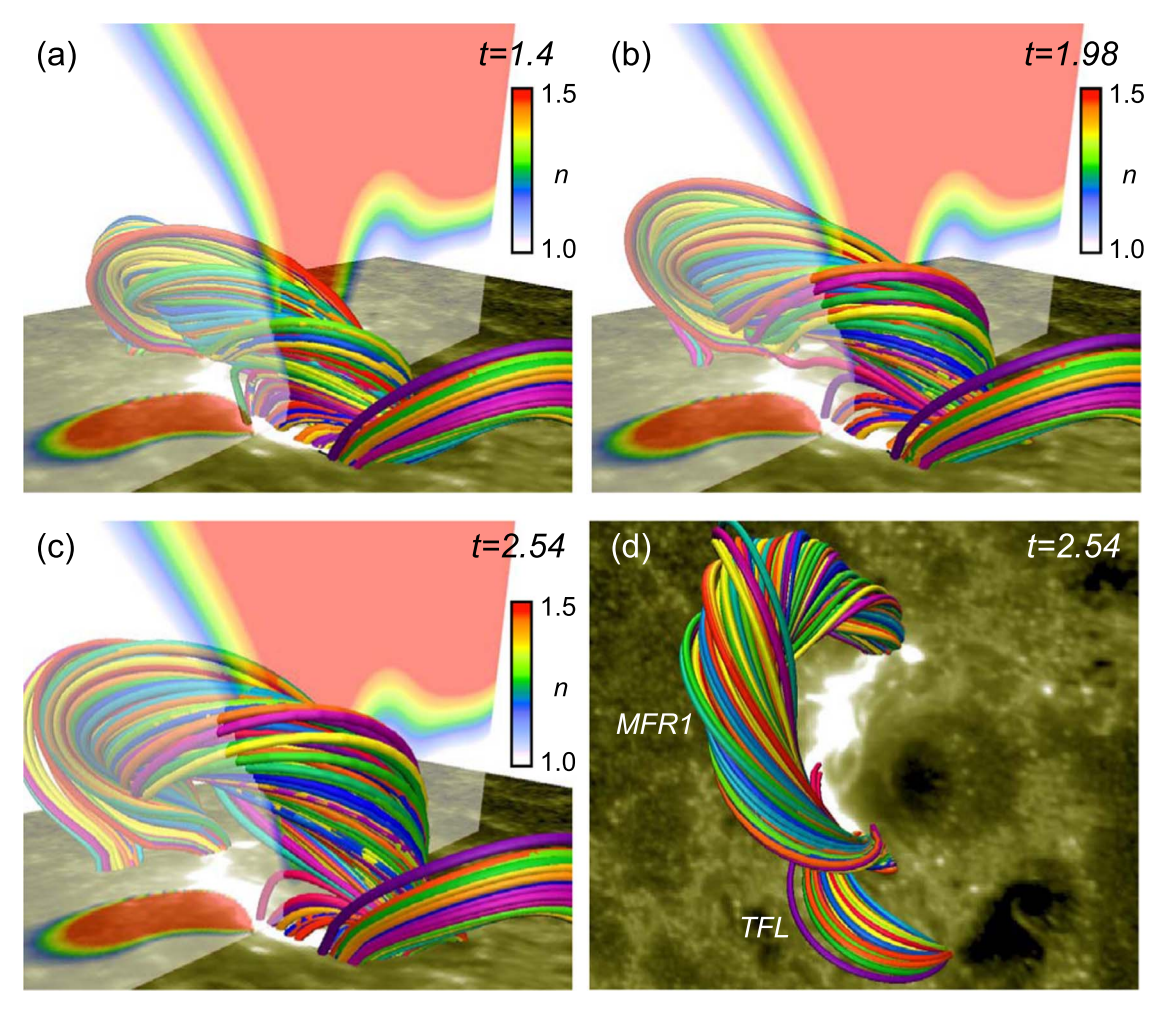


Figure 8. (a)—(c) Evolution of the erupting MFR from t = 1.4—2.54 and the distribution of the decay index derived from the potential field. In this period, the speed of the rise of the MFR switches from slow to fast. The bottom corresponds to the AIA 1600 Å image taken at $t_{\rm obs} = 11:54:28$ UT, which corresponds to the early stage of the X9.3 flare. (d) The top view of (c).

lines through reconnection. Afterward, as seen in Figure 3, the FUV brightening is strongly enhanced and extended southward. In this simulation, the erupting MFR, named "MFR1," in Figure 8(d), reconnects with the twisted field lines named "TFL" during the eruption. Consequently, the large MFR is formed as shown in Figure 6(a), and one footpoint of the newly created MFR is anchored in the brightening region extending southward, as seen in AIA 1600 Å. Therefore, this simulation offers a sound explanation of the behavior of the 1600 Å images observed in the X9.3 flare.

4. Discussion

4.1. A Possibility of Another Scenario for the Solar Eruption

4.1.1. Another Candidate Triggering Solar Eruption

In the previous sections, we have demonstrated that the reconnection occurring at a local area, where the negative polarity intrudes into the opposite one (see Figure 1(c)), is important to produce the X2.2 flare. Further continuous reconnection drives the evolution of the MFR and eventually causes the X9.3 flare. We now discuss another scenario to produce the successive flares. Because AR 12673 shows a very complex magnetic field distribution, magnetic null points are likely to exist at several points. For example, Figures 9(a) and (b) (top views in

Figures 9(c) and (d)) show the location of the null points via purple field lines and yellow field lines. The location of null point A corresponds to the one marked by the dashed circle in Figure 4(c). Our simulation suggested that the X-flares are produced here, and this was also supported by several previous studies (e.g., Bamba et al. 2020; Price et al. 2019; Zou et al. 2020). On the other hand, another null point, B, which is farther away from null point A, is also reported in Mitra et al. (2018), Zou et al. (2019). This might have the potential to cause a flare and an eruption. In this section, we discuss the possibility of flare triggering via reconnection in a different area from where the intruding motion was observed, such as in null point B.

To test this hypothesis, we perform another MHD simulation using the NLFFF reconstructed from the photospheric magnetic field, recorded at 02:36 UT on September 6. This simulation is named "Run B," while the previous one is denoted "Run A." In this study, the flare-triggering reconnection in Run A is excited by the numerical resistivity in the strong current region, due to the strong intruding motion of the negative polarity. Figures 10(a) and (b) exhibit the distribution of B_z observed at 02:36 UT and 08:36 UT, respectively, from which it is seen that the intrusion of the negative polarity has not fully taken place at 02:36 UT. Therefore, as of 02:36 UT, we expect that the reconnection should be suppressed at the region where the strong intruding motion was

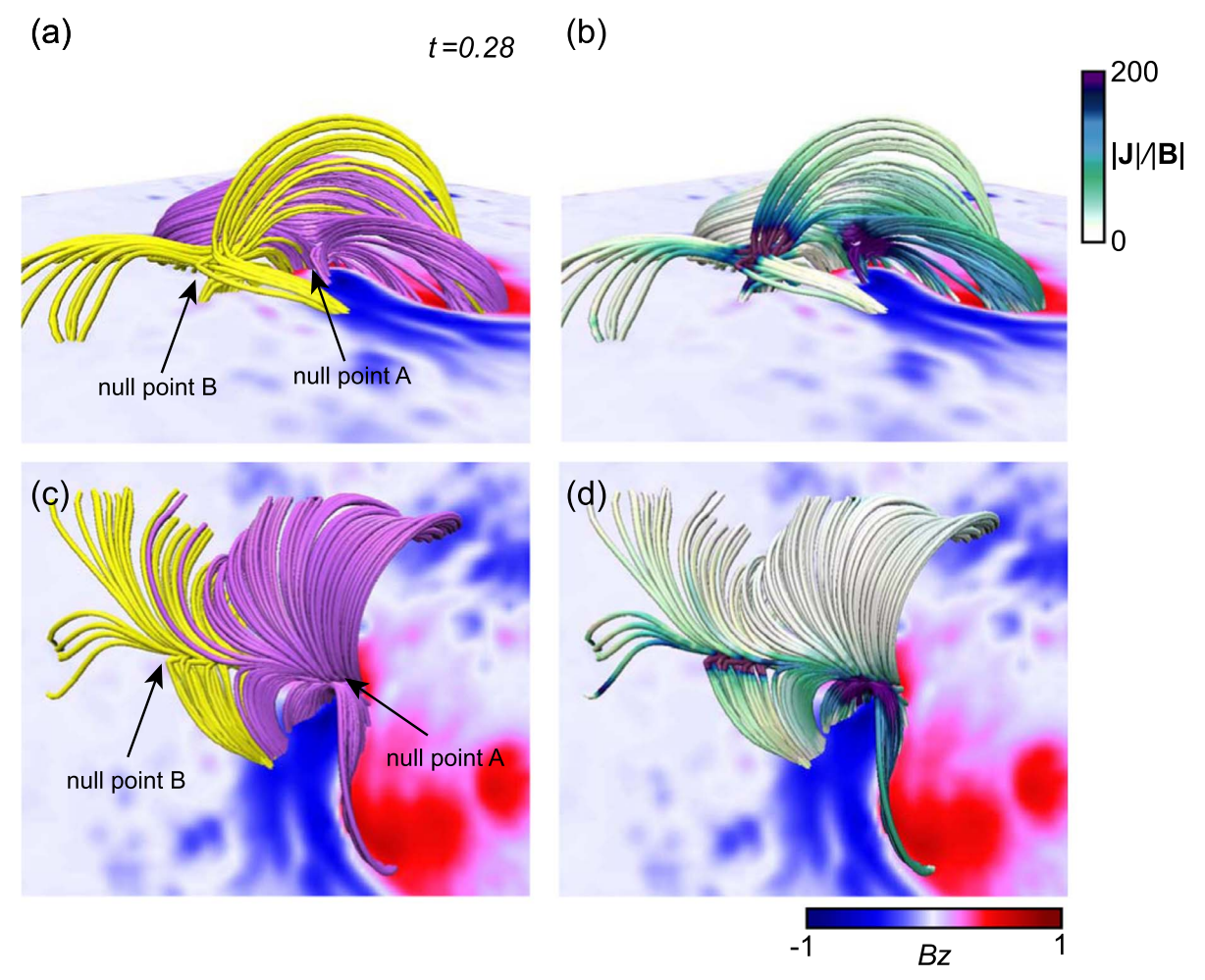


Figure 9. (a) The field lines at t = 0.28 just before the X2.2 flare. Null point A is found in the purple field lines, which correspond to those in Figure 4(c). Another null point, B, is shown by the yellow field lines. (b) The magnetic field lines are colored by the value of |J|/|B|. The strong value is enhanced at each null point. (c), (d) The top view of (a) and (b).

observed later. Figures 10(c) and (d) show the results of the magnetic twist, T_w , obtained from the two NLFFFs reconstructed at t=02:36 and 08:36, respectively, and a quantitative comparison is shown in Figure 10(e). These distributions of T_w are similar in both cases, but the value obtained at 08:36 UT is higher than the one at 02:36 UT. Figure 10(f) shows the field lines at t=0.28 obtained from the MHD simulation when the NLFFF reconstructed at 02:36 UT is used as the initial condition, in which we can find the two regions of steep gradient of the magnetic field, marked by the dashed yellow and red circles, because |J|/|B| is strongly enhanced there. These locations are similar to those shown in Figure 9 while the magnetic configuration at 02:36 UT is different from the one at 08:36 UT. From our results, the X2.2 flare appeared at the area indicated by the yellow circle when we used the photospheric magnetic field obtained 6 hr later.

4.1.2. Two Different Solar Eruptions

The field lines constituting the MFR and |J|/|B| distribution on the vertical cross section for Runs A and B are plotted in Figures 11(a) and (b), respectively. In both cases, the MFR is formed and the patterns of |J|/|B| are similar to each other. In Run B, however, the location of the current sheet formed under the MFR slightly deviates from the region where the strong intruding motion is observed while being enhanced above the

region in Run A. Therefore, these results suggest that the reconnection region is different between Run A and Run B. Specifically, the reconnection in Run B does not take place at the region intruded on by the negative polarity. Figures 11(c) and (d) show snapshots of the 3D magnetic field lines obtained in Run B from the top and side views, respectively. The field lines colored according to |J|/|B| are traced from the region around the current sheet, following which the reconnection occurs outside of the highly twisted lines. This location corresponds to the region indicated by the red dashed circle in Figure 10(f) and the MFR can be created here, although it takes a longer time to make the MFR compared to Run A.

Interestingly, both Runs A and B exhibited eruptions albeit driven by different reconnections, which take place at different locations: one is due to the intrusion of the negative polarity in Run A and the other is due to the reconnection at a different location, which is away from the region of the intruding motion of the sunspot, in Run B. In this event, as shown in Figures 4(e) and (f), the strong brightening was observed at the beginning of the X2.2 flare at the region of the intruding motion of the sunspot. Furthermore, from Figures 4(a) and (b), the footpoints of the field lines are anchored well on the strong brightening region of AIA 1600 Å, which are not the field lines connecting close to the null point of the magnetic field

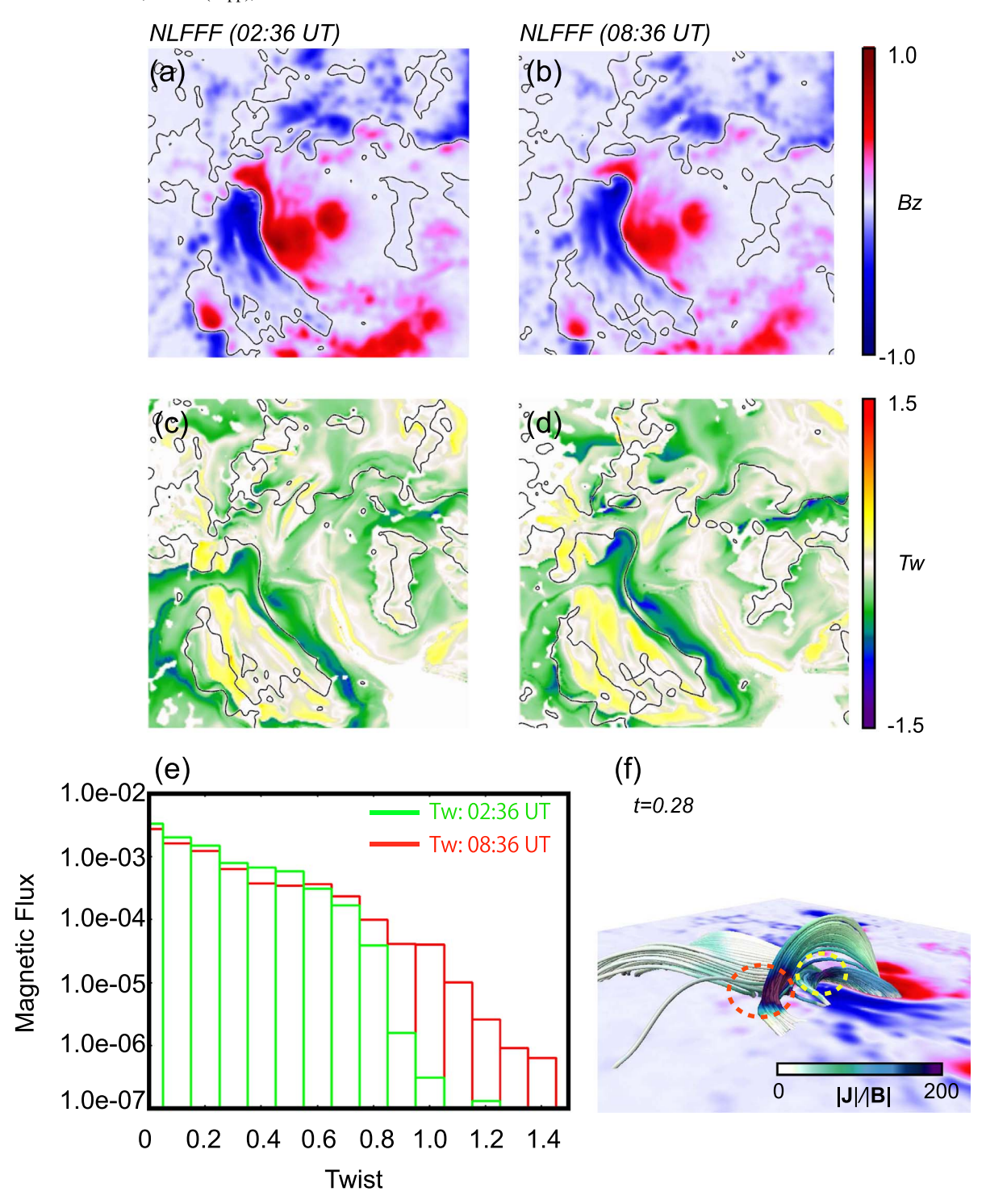


Figure 10. (a), (b) B_z distribution observed at t=02:36 UT and t=08:36 UT, respectively, where the black line corresponds to a contour of $B_z=0$. (c), (d) Magnetic twist T_w of each field line mapped on the photosphere at t=02:36 UT and t=08:36 UT, respectively. (e) Histogram of magnetic flux vs. twist where the green and red lines are calculated from the NLFFF reconstructed at t=02:36 UT and t=08:36 UT, respectively. (f) The magnetic field obtained from the MHD simulation at t=0.28 when the NLFFF reconstructed at 02:36 UT is used. The color of the field lines corresponds to the value of |J|/B|.

indicated by the red dashed circle shown in Figure 10(f). If the eruption in Run B occurs, the flare brightening observed in the AIA 1600 Å observations would appear at the location outside of the highly twisted lines because they are surrounded by field lines participating in the reconnection.

From the above, we confirm the possibility of another eruption that is different from the observed one. Moreover, it would be possible 6 hr before the X2.2 flare was

observed. Yamasaki et al. (2021) pointed out that the highly twisted field lines, which produce the X-flares, are already formed as of 2 days before and suggested that the strong intrusion of the sunspot plays an important role in breaking the stable magnetic field through the reconnection. Because the value of electric resistivity is considered to be very small in the solar corona, the reconnection does not happen so easily in that situation unless the MFR becomes unstable

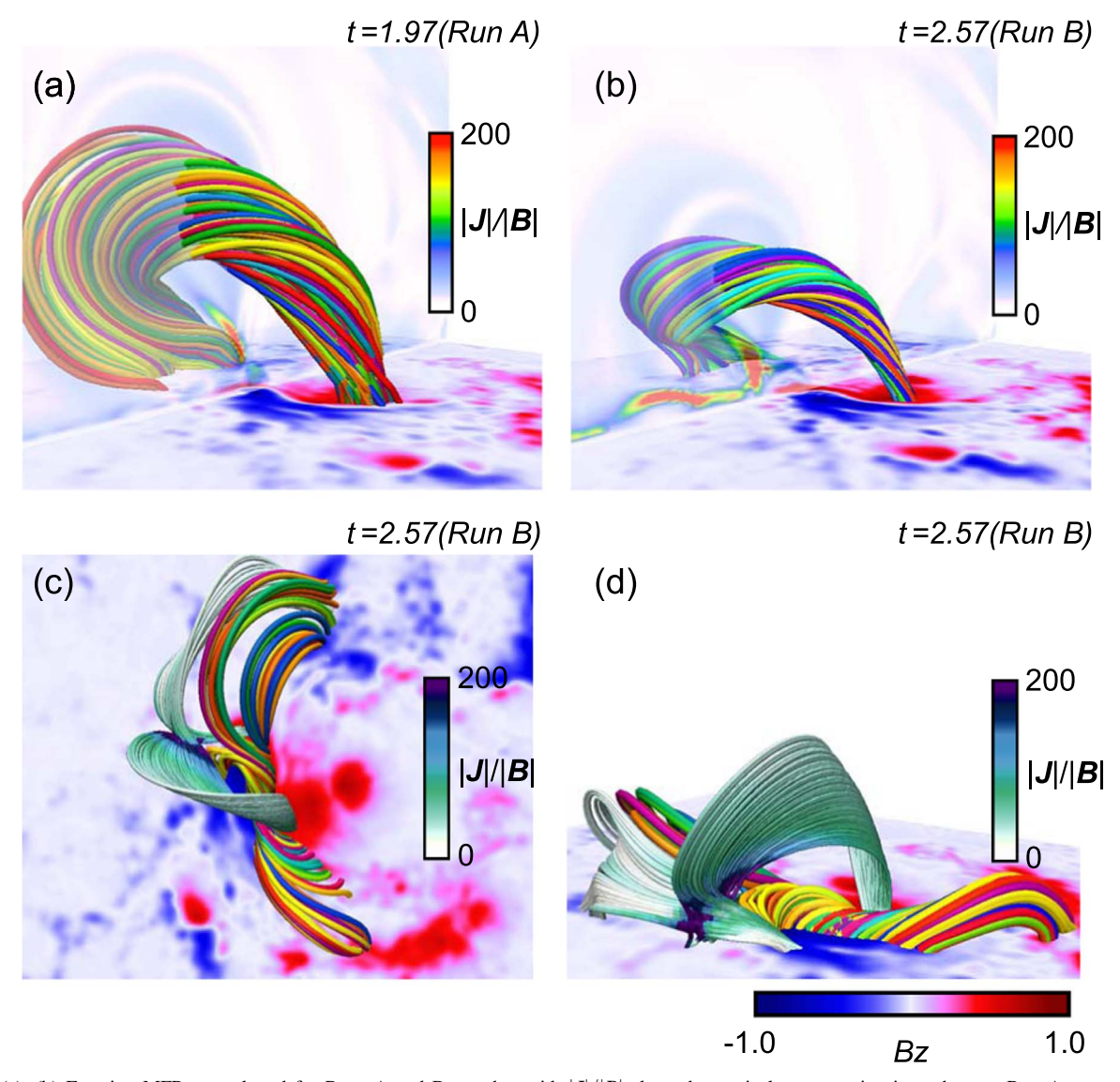


Figure 11. (a), (b) Erupting MFRs are plotted for Runs A and B together with |J|/|B| along the vertical cross section in each case. Run A corresponds to the simulation started with the NLFFF reconstructed at 08:36 UT, while Run B corresponds to that reconstructed at 02:36 UT. The location of the current sheet formed under the MFR is different between Run A and Run B. (c), (d) The snapshots of magnetic field lines at t = 2.57 in Run B from the top and side views, respectively. The field lines, drawn from the value of |J|/|B| and traced from the region around the current sheet, surround the highly twisted lines existing above PIL.

or the photospheric motion drives the upper magnetic field connecting the null point. In other words, if these would instead have taken place in the area where null point B exists, a different eruption before the X-flares might have taken place.

4.2. Gap between the Observation and the Simulation

We finally mention an inconsistency between the observations and the simulation. As shown in Figure 1(c), the negative polarity starts the intrusion into the neighboring positive polarity before the occurrence of the X2.2 flare. From the detailed analysis of the observational data, Bamba et al. (2020) indicate that the intrusion is a major candidate for driving the first flare (X2.2). When the negative polarity continuously intrudes into the neighboring opposite polarity, it can drive flux cancellation. This creates the MFR through reconnection and eventually leads to the triggering of the second flare (X9.3). Although the overview is similar between the observation and the simulation, we used a snapshot of the magnetic field in this

study, which is taken before the X2.2 flare, as the boundary condition of our MHD simulation. Thus, we cannot discuss the phenomena along the temporal evolution of the photospheric magnetic field, e.g., the energy buildup process after the X2.2 flare reported in Zou et al. (2020). In our simulation, the reconnection starting the X2.2 flare and after that is driven by numerical resistivity instead of by photospheric magnetic cancellation through the intrusion.

5. Summary

In order to reveal the MHD process of the successive flares observed on 2017 September 6, we performed a data-constrained MHD simulation using NLFFF, which is reconstructed before the X2.2 flare, as the initial condition of the simulation. As shown in Figure 5, the twisted lines igniting the X2.2 flare are sandwiched by those causing the X9.3 flare. The X2.2 flare removes part of the innermost field lines; consequently, twisted lines existing at the outside form the basis of the MFR through reconnection as shown in the inset of Figure 5(b). The MFR is enhanced, in particular its

twist and size, and lifted up through continuous reconnection after the X2.2 flare. The MFR eventually experiences TI, which triggers the eruption and gives rise to the X9.3 flare. In this simulation we used one snapshot of the photospheric magnetic field, which is prior to the X2.2 flare; therefore, we cannot trace the evolution of the photospheric motion taking place between the X2.2 to X9.3 flares, and our simulation cannot take on the phenomena derived from the time-dependent boundary motion, namely, the shearing and intruding motion of the negative polarity. For further development, data-driven simulation (Toriumi et al. 2020) would be useful to cover the dynamics derived from the time-dependent boundary condition.

We confirmed another scenario for the eruption due to reconnection, which takes place away from the region where the intruding motion of the sunspot was observed, by using the NLFFF 6 hr 30 minutes before the X2.2 flare. Although this scenario hardly explains the AIA 1600 Å observations, this result indicated that the eruption might be achieved at the different than where the X2.2 flare was observed. Yamasaki et al. (2021) pointed out that the strong twist of the field lines already accumulated in the magnetic field 2 days before the X2.2 flare, so the intruding motion of the sunspot is important to break the stable magnetic field and cause the X2.2 flare. On the contrary, if some kind of disturbance is imposed on the region where the magnetic field connecting the null point exists, another eruption might happen. As in this AR, there are several possibilities for eruptions in ARs that have a complex magnetic field. Therefore, it is important to detect the disturbance as the triggering process of the solar flare (Bamba et al. 2013; Wang et al. 2017; Bamba & Kusano 2018; Kang et al. 2019) and to understand the physical property of the 3D magnetic structure (Kusano et al. 2020) as well as the magnetic topology for correctly predicting the solar flares. In addition, as a further interesting issue, how different are the large flares produced depending on reconnection taking place at different areas? We hope to address this topic in future work.

We are grateful to the anonymous referee for many constructive comments and carefully checking the manuscript. We thankful to Dr. Sung-Hong Park for supporting the CEA projection of the AIA images. SDO is a mission of NASA's Living With a Star Program. This work was supported by MEXT/JSPS KAKENHI, grant No. JP15H05814 and MEXT as "Exploratory Challenge on Post-K computer" (Elucidation of the Birth of Exoplanets [Second Earth] and the Environmental Variations of Planets in the Solar System). This work was also supported by "Nagoya University High Performance Computing Research Project for Joint Computational Science" in Japan and the Center for Integrated Data Science of Institute of Space-Earth Environmental Research, Nagoya University. The research is partially supported by the National Science Foundation under grant AGS-1954737. The visualization was performed by VAPOR (Clyne & Rast 2005; Clyne et al. 2007).

ORCID iDs

Satoshi Inoue https://orcid.org/0000-0001-5121-5122 Yumi Bamba https://orcid.org/0000-0001-8385-8990

References

```
Amari, T., Luciani, J. F., Mikic, Z., et al. 1999, ApJL, 518, L57
Aulanier, G., Janvier, M., & Schmieder, B. 2012, A&A, 543, A110
Bamba, Y., Inoue, S., & Imada, S. 2020, ApJ, 894, 29
Bamba, Y., & Kusano, K. 2018, ApJ, 856, 43
Bamba, Y., Kusano, K., Yamamoto, T. T., et al. 2013, ApJ, 778, 48
Bateman, G. 1978, MHD Instabilities (Cambridge, MA: MIT Press)
Berger, M. A., & Prior, C. 2006, JPhA, 39, 8321
Bobra, M. G., Sun, X., Hoeksema, J. T., et al. 2014, SoPh, 289, 3549
Clyne, J., Mininni, P., Norton, A., et al. 2007, NJPh, 9, 301
Clyne, J., & Rast, M. 2005, Proc. SPIE, 5669, 284
Dedner, A., Kemm, F., Kröner, D., et al. 2002, JCoPh, 175, 645
Gordovskyy, M., Browning, P. K., Inoue, S., et al. 2020, ApJ, 902, 147
Guo, Y., Cheng, X., & Ding, M. 2017, ScChD, 60, 1408
Hou, Y. J., Zhang, J., Li, T., et al. 2018, A&A, 619, A100
Inoue, S. 2016, PEPS, 3, 19
Inoue, S., Hayashi, K., Magara, T., et al. 2014, ApJ, 788, 182
Inoue, S., Kusano, K., Büchner, J., et al. 2018, NatCo. 9, 174
Inoue, S., Magara, T., Pandey, V. S., et al. 2014, ApJ, 780, 101
Inoue, S., Shiota, D., Bamba, Y., et al. 2018, ApJ, 867, 83
Janvier, M., Aulanier, G., Pariat, E., et al. 2013, A&A, 555, A77
Jenkins, J. M., Hopwood, M., Démoulin, P., et al. 2019, ApJ, 873, 49
Jiang, C., Zou, P., Feng, X., et al. 2018, ApJ, 869, 13
Kang, J., Inoue, S., Kusano, K., et al. 2019, ApJ, 887, 263
Kliem, B., & Török, T. 2006, PhRvL, 96, 255002
Kusano, K., Iju, T., Bamba, Y., et al. 2020, Sci, 369, 587
Lemen, J. R., Title, A. M., Akin, D. J., et al. 2012, SoPh, 275, 17
Lin, P. H., Kusano, K., Shiota, D., et al. 2020, ApJ, 894, 20
Liu, L., Cheng, X., Wang, Y., et al. 2018, ApJL, 867, L5
Liu, R., Kliem, B., Titov, V. S., et al. 2016, ApJ, 818, 148
Lumme, E., Pomoell, J., & Kilpua, E. K. J. 2017, SoPh, 292, 191
Lysenko, A. L., Anfinogentov, S. A., Svinkin, D. S., et al. 2019, ApJ, 877, 145
Mitra, P. K., Joshi, B., Prasad, A., et al. 2018, ApJ, 869, 69
Olmedo, O., & Zhang, J. 2010, ApJ, 718, 433
Pesnell, W. D., Thompson, B. J., & Chamberlin, P. C. 2012, SoPh, 275, 3
Price, D. J., Pomoell, J., Lumme, E., et al. 2019, A&A, 628, A114
Priest, E. R., & Forbes, T. G. 2002, A&ARv, 10, 313
Romano, P., Elmhamdi, A., & Kordi, A. S. 2019, SoPh, 294, 4
Sakurai, T. 1982, SoPh, 76, 301
Scherrer, P. H., Schou, J., Bush, R. I., et al. 2012, SoPh, 275, 207
Scolini, C., Chané, E., Temmer, M., et al. 2020, ApJS, 247, 21
Threlfall, J., Hood, A. W., & Priest, E. R. 2018, SoPh, 293, 98
Toriumi, S., Takasao, S., Cheung, M. C. M., et al. 2020, ApJ, 890, 103
Toriumi, S., & Wang, H. 2019, LRSP, 16, 3
Török, T., Kliem, B., & Titov, V. S. 2004, A&A, 413, L27
Vemareddy, P. 2019, ApJ, 872, 182
Wang, H., Liu, C., Ahn, K., et al. 2017, NatAs, 1, 0085
Wang, R., Liu, Y. D., Hoeksema, J. T., et al. 2018, ApJ, 869, 90
Wiegelmann, T., Inhester, B., & Sakurai, T. 2006, SoPh, 233, 215
Wiegelmann, T., & Sakurai, T. 2012, LRSP, 9, 5
Wu, C.-C., Liou, K., Lepping, R. P., et al. 2019, SoPh, 294, 110
Yamasaki, D., Inoue, S., Nagata, S., et al. 2021, ApJ, 908, 132
Yan, X. L., Wang, J. C., Pan, G. M., et al. 2018, ApJ, 856, 79
Yang, S., Zhang, J., Zhu, X., et al. 2017, ApJL, 849, L21
Zou, P., Jiang, C., Feng, X., et al. 2019, ApJ, 870, 97
Zou, P., Jiang, C., Wei, F., et al. 2020, ApJ, 890, 10
Zuccarello, F. P., Aulanier, G., & Gilchrist, S. A. 2015, ApJ, 814, 126
```